

Banner appropriate to article type will appear here in typeset article

Identifying skin-friction generation structures in turbulent channel flows via canonical correlation decomposition

Ziyi Nie, Jie Yao^{2†} and Benshuai Lyu^{1‡}

¹State Key Laboratory of Turbulence and Complex Systems, School of Mechanics and Engineering Science, Peking University, Beijing 100871, China.

²School of Interdisciplinary Science, Beijing Institute of Technology, Beijing, 100081, China.

(Received xx; revised xx; accepted xx)

Flow structures directly responsible for local skin-friction generation in turbulent channel flows are identified using the newly developed Canonical Correlation Decomposition (CCD) method. The dominant structures take the form of streamwise streaks that are spanwise-localised around the position where the skin-friction is targeted and exhibit significantly shorter streamwise extent than those revealed using POD. The resulting CCD spectrum shows a clear low-rank behaviour; flow reconstruction using only the first 4 CCD modes recovers more than 80% of the examined skin friction, as opposed to 2% recovered by the leading 4 POD modes. When the opposition control technique is used to reduce drag, the application of CCD shows that drag reduction is achieved by lifting the original streak structures and generating smaller streaks with opposite phases underneath. These findings demonstrate that CCD isolates the causally relevant flow structures governing skin-friction generation and modification, which is expected to find use in various drag control applications in wall-bounded turbulence.

1. Introduction

Skin-friction drag in wall-bounded turbulence significantly surpasses its laminar counterpart at equivalent Reynolds numbers (Kim 2011). In particular, it constitutes up to 50% of the total drag on commercial aircraft, nearly 90% for submarines, and almost all drag for internal flows (e.g., pipes/channels). Therefore, understanding the physical mechanisms responsible for skin-friction generation and developing effective drag control strategies are of central importance for energy efficiency and environmental sustainability (Gad-el Hak 2007).

Although skin friction is inherently a wall property, defined based on the wall-normal gradient of the streamwise velocity, it is intimately connected with flow physics across the entire wall layers. Over the past decades, a variety of decomposition frameworks have been proposed to relate the mean skin-friction coefficient to statistical flow quantities. For example, the seminal contribution of Fukagata *et al.* (2002), widely known as the FIK identity, expresses the mean skin-friction coefficient in terms of the Reynolds shear-stress distribution in wall-bounded turbulence. An alternative viewpoint was later provided by Renard & Deck (2016), which interprets skin friction as the rate at which energy is transferred from the wall to the fluid through viscous dissipation and turbulence production. Building

† Co-first author; the first two authors contribute equally.

‡ Email address for correspondence: b.lyu@pku.edu.cn

on these two pioneering identities, numerous extensions have recently been developed (Yoon *et al.* 2016; de Giovanetti *et al.* 2016; Chen *et al.* 2021), significantly advancing our understanding of skin friction generation and drag-reduction mechanisms in wall-bounded flows (Elnahhas & Johnson 2022; Ricco & Skote 2022; Floryan 2023; Zhao *et al.* 2024).

Despite the progress enabled by existing decomposition frameworks, they focus primarily on mean or statistical quantities and therefore cannot identify the corresponding flow structures that generate the skin friction. It is well-established that the skin-friction drag in wall turbulence arises predominantly from the near-wall self-sustaining cycle, namely, the regeneration of streamwise streaks and vortices. Therefore, most drag-reduction strategies aim to weaken or disrupt these quasi-coherent motions (Rastegari & Akhavan 2018; Gatti & Quadrio 2016). At high Reynolds numbers, however, recent studies have demonstrated that large-scale and very-large-scale outer motions play an increasingly important role in contributing to the wall shear stress (Marusic *et al.* 2021), suggesting that skin-friction generation results from a multiscale structural organisation spanning the entire wall layer. To probe the structural sources of the skin friction generation, prior efforts have largely relied on correlation-based analyses or conditional averaging techniques (Jeong *et al.* 1997; Hwang 2015). Despite important insights revealed by these methods, the connection between such flow structures and skin friction remains largely qualitative. This underscores the need for a unified framework that quantitatively relates coherent flow structures to skin-friction generation, with which a more mechanistic understanding may be obtained while consistent comparisons among different control strategies can be made (Yao *et al.* 2018).

To achieve this goal, modal decomposition techniques may be used. Common decomposition techniques such as the Proper Orthogonal Decomposition (POD) and Direct Mode Decomposition (DMD), are widely used to extract coherent structures from complex turbulent flows. The resulting POD modes are ranked by their kinetic energy content, while DMD modes are ordered in terms of their “contribution” to the overall dynamics of the underlying system. However, our interests are not to seek energetic or dynamically dominant structures, but rather those that contribute most directly to skin-friction generation. Because neither POD nor DMD is designed to target wall shear stress, a large number of modes is typically required to reconstruct the instantaneous skin friction with reasonable accuracy. Recently, Canonical Correlation Decomposition (CCD) (Lyu 2024a,b) has been proposed as an observable-targeted decomposition technique that isolates flow structures most strongly correlated with a given quantity of interest, while suppressing uncorrelated contributions. This property makes CCD particularly well-suited for identifying the structures directly responsible for skin-friction generation. The main objective of the present work is to apply CCD to turbulent channel flows to extract and characterise these structures.

The paper is structured as follows. Section 2 outlines the CCD methodology and describes direct numerical simulation (DNS) databases of turbulent channel flows used. Section 3 shows the resulting flow structures that are most correlated with skin friction. The analysis is then extended to channel flows subject to opposition control, allowing the structural modifications associated with reduced drag to be examined. The following section concludes the paper.

2. CCD of turbulent channel flows

As demonstrated by Lyu (2024a,b), CCD aims to decompose the flow field based on its correlation strength with a given observable. For the sake of self-completeness, we outline the essential steps to perform the CCD. Consider a sequence of snapshots \mathbf{u}_i obtained by sampling a flow field $\mathbf{u}(\mathbf{x}, t)$ at time $t = t_i$, where \mathbf{x} represents the coordinates of the flow domain, and i is an integer that takes the value of $1, 2, 3, \dots, N$. Suppose that each snapshot is represented by a column vector of length M after spatial discretisation. We write this snapshot sequence compactly in a matrix notation as $\mathbf{U} = [\mathbf{u}_1, \mathbf{u}_2, \mathbf{u}_3, \dots, \mathbf{u}_N]$.

For each t_i used to sample \mathbf{u}_i , assume that one can simultaneously sample an observable $p(t)$ at time $t_i + \tau_j$ and obtain the sequence $p_{i,j}$, $j = 1, 2, 3 \dots Q$, where j is an integer and takes

the values of $1, 2, 3, \dots, Q$ (Q being a positive integer). In most cases, where the observable is not significantly behind or ahead of the flow, one can assume $\tau_1 \approx -\tau_Q/2$ for simplicity. For each integer i , one defines a column vector $\mathbf{p}_i = [p_{i,1}, p_{i,2}, p_{i,3}, \dots, p_{i,Q}]^T$, where T denotes transpose. These vectors can be assembled into a matrix $\mathbf{P} = [\mathbf{p}_1, \mathbf{p}_2, \dots, \mathbf{p}_{N-1}, \mathbf{p}_N]$.

CCD starts by constructing the correlation matrix \mathbf{A} and performing the singular value decomposition according to

$$\mathbf{A} = (1/\sqrt{QN^2})\mathbf{P}\mathbf{U}^\dagger = \mathbf{R}\Sigma\mathbf{V}^\dagger, \quad (2.1)$$

where \dagger denotes Hermitian adjoint (complex transpose), and Σ is a diagonal matrix with the singular values σ_j ($j = 1, 2, 3, \dots, \min(M, Q)$) as its diagonal elements. The column vectors of \mathbf{V} represent the CCD modes of the flow field; these modes are mutually orthogonal, ranked by their correlation strength with the observable (σ_j^2).

To identify the flow structures most correlated with the skin friction, CCD is applied to several high-fidelity DNS databases of turbulent channel flows, performed using the code developed by [Lee & Moser \(2015\)](#). First, two regular uncontrolled turbulent channel flows at friction Reynolds numbers of $Re_\tau (\equiv u_\tau h/\nu) \approx 180$ and 550 , respectively, are considered. In addition, a database of opposition control with detection plane $y_d^+ = 15$ at $Re_\tau \approx 180$ [Yao et al. \(2025\)](#) is included to examine how drag reduction modifies the correlation-based structures. For all cases, the computational domain size is $4\pi h \times 2h \times 2\pi h$ in the streamwise (x), wall-normal (y) and spanwise (z) directions, respectively, where h denotes the half-channel-height. The flow is driven by a pressure gradient, which varies in time to ensure that the mass flux through the channel remains constant. The simulation time step is fixed at $\Delta t = 0.01h/U_b$ for the two databases of $Re_\tau \approx 180$, while it is fixed at $\Delta t = 0.005h/U_b$ for $Re_\tau \approx 550$. The flow snapshots are stored every 100 time steps, while the skin friction is stored every 10 time steps for all the databases.

For the decomposition, the streamwise velocity is chosen to represent the flow field. The observable is the skin-friction coefficient c_f at the centre of the bottom plate, i.e. $(x, y, z) = (0, 0, 0)$. To improve statistical convergence in the calculation of the correlation matrix \mathbf{A} , statistical homogeneity of the flow is exploited. This is because any point on the wall is equally suitable as an observable location; the associated coherent structures for all observables are identical up to a spatial shift. Thus, multiple observables may be used by spatially shifting the velocity field relative to the observable location. For example, for c_f at $(0, 0, 0)$, the unshifted velocity field is used, whereas for c_f at $(\pi, 0, 0)$, the velocity field is circularly shifted by π in the streamwise direction and used as an additional sample in the ensemble space. In this study, 192 such observables are employed, substantially improving the statistical convergence of the resulting CCD modes.

Note that for CCD, the sampling frequency of the observable is independent of that of the flow. Here it is sampled ten times faster for all databases to better resolve the temporal correlation. For example, in the uncontrolled $Re_\tau \approx 180$ case, a total of 16870 c_f samples are obtained, while only 1687 velocity snapshots are used. Since the correlation between the flow and observable are likely to decay to zero beyond a time shift of $10h/U_b$, we choose Q to be 100. Since the temporal delay between the flow and the observable is negligible, we choose τ_1 to be $-5\Delta t_s$. For comparison, a POD analysis is also performed.

3. Results and Discussion

In this section, the CCD analysis is applied to three DNS datasets: two uncontrolled cases at $Re_\tau \approx 180$ and 550 respectively, and a drag-reduction case with opposition control at $Re_\tau \approx 180$. For each case, we examine the CCD spectra and the corresponding modes that are most strongly correlated with the instantaneous wall shear stress. The spectra and mode shapes from the POD are also briefly presented for comparison.

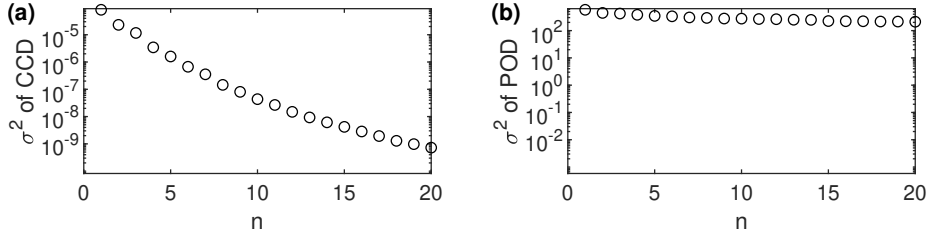


Figure 1: The spectra of (a) CCD and (b) POD modes when $Re_\tau \approx 180$.

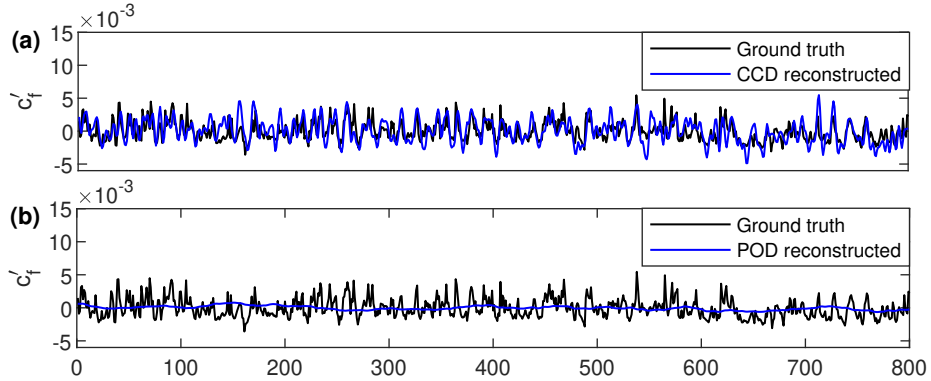


Figure 2: Reconstruction of the skin friction coefficient (fluctuation part) using the first 4 CCD (a) and POD (b) modes when $Re_\tau \approx 180$, respectively.

3.1. Uncontrolled cases at $Re_\tau \approx 180$ and 550

Figure 1 shows the spectra of the first 20 CCD and POD modes for uncontrolled $Re_\tau \approx 180$ case. Note that for CCD modes, the singular values squared σ_j^2 measure the correlation strength between the observable and each mode, whereas for POD, they reflect the kinetic energy of each mode. Compared with POD, the CCD spectrum exhibits a much steeper decay as mode number n increases, indicating a possibility of effective order reduction. In particular, figure 1(a) shows that only the first few CCD modes possess significant correlation with the skin friction. By contrast, the POD spectrum remains comparatively flat, indicating that the kinetic energy of POD modes decays too slowly to yield an efficient reduced-order representation of the total flow.

The rapid decay of the CCD spectrum suggests that the skin friction may be well approximated by a low-rank model built from only a few leading CCD modes. Such an attempt is demonstrated in figure 2, which shows reconstructions of the instantaneous skin-friction coefficient c_f obtained by projecting the flow field onto the first four CCD or POD modes. Specifically, for flow field \mathbf{u}_i at time t_i , its projection on k -th order mode \mathbf{v}_k is calculated by $a_k(t_i) = \mathbf{u}_i \mathbf{v}_k$. Thus, an approximation of \mathbf{u}_i is obtained using the linear combination of the first 4 modes, i.e. $\mathbf{u}'_i = \sum_{k=1}^4 a_k(t_i) \mathbf{v}_k$.

The skin friction coefficient c_f is then reconstructed using Newton's law by calculating the wall-normal gradient of the reconstructed streamwise velocity at the observer point. Figure 2(a) shows that the reconstruction based on the first four CCD modes closely follows the ground truth. More specifically, the reconstruction recovers more than 80% of c_f variation under the L_2 norm. As the sampling frequency of the observable increases, an even higher accuracy may be expected. In contrast, the reconstruction using the first four POD modes (figure 2(b)) performs poorly. This is anticipated, as since POD ranks structures by kinetic energy rather than by their contribution to c_f variations. In summary, figures 1 and 2

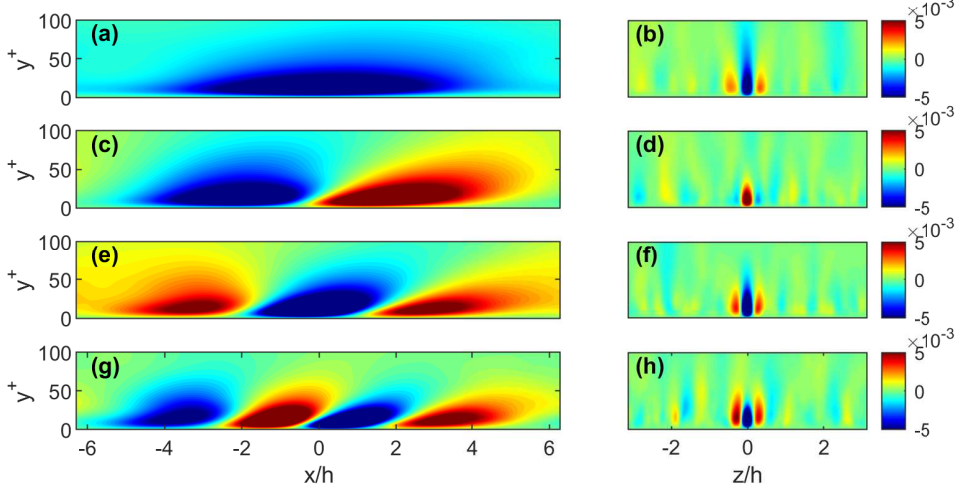


Figure 3: Front (a, c, e, g) and left (b, d, f, h) views of the first four CCD modes when $Re_\tau \approx 180$. $z = 0$ for (a, c, e, g) while $x = 0$ for (b, f) and $x = 1/3\pi$ for (c, h).

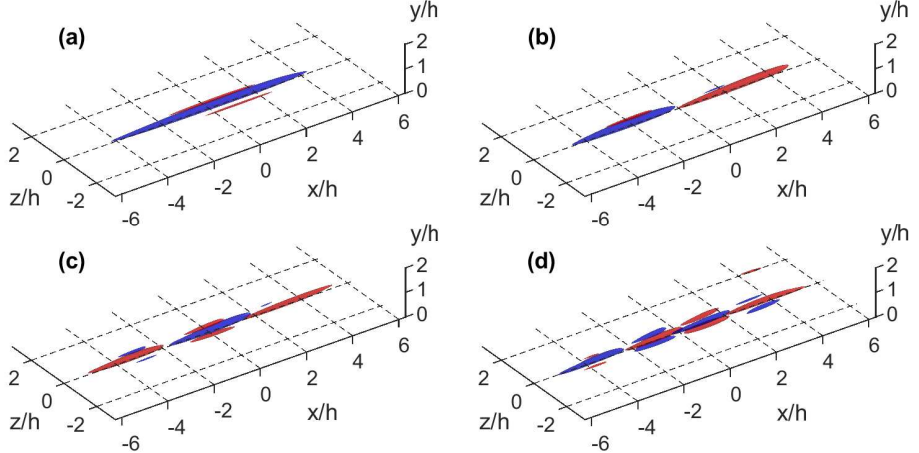


Figure 4: Isosurface of the 1st- to 4th- order (a to d) CCD modes when $Re_\tau \approx 180$. The red and blue isosurfaces represent 50% and -50% of the fluctuation amplitude, respectively.

demonstrate that CCD provides a markedly more compact representation of the c_f -producing structures compared with PODs.

We are now in a position to examine the spatial structures of the resulting CCD and POD modes. They are shown in figures 3 to 5, respectively. The two decompositions yield significantly different structures in both location and organisation.

Figures 3(a,c,e,g) show the front (x - y plane) views of the first four CCD modes. The CCD modes take the form of streamwise-elongated streaks whose centres are aligned with the observable location on the bottom wall. These streaks appear at a finite distance above the wall, whose centres are located at approximately $y^+ \approx 15$. This height is consistent with the well-established position of the buffer-layer streaks that dominate momentum transfer and near-wall shear production in canonical wall turbulence. The leading-order CCD mode exhibits the largest streamwise coherence, whereas higher-order modes display progressively shorter characteristic wavelengths, as manifested by the increasingly rapid phase variations.

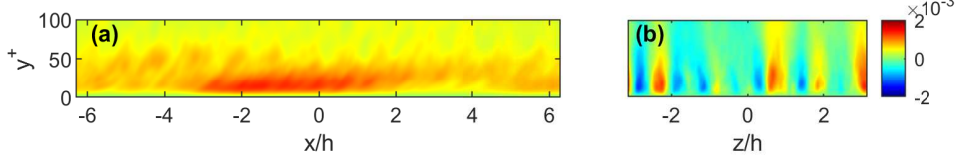


Figure 5: Front (a) and left (b) views of the first POD mode when $Re_\tau \approx 180$. $z = 0.6$ for (a) while $x = 0$ for (b).

The streaks are also slightly inclined in the x - y plane, a feature commonly associated with the growth and lifting of coherent packets or hairpin-like vortical structures.

Figures 3(b,d,f,h) provide the corresponding side (y - z plane) view of the first four CCD modes. In the spanwise direction, the CCD modes are strongly localised around the observable point at $z = 0$. Their effective spanwise width is approximately $0.2h$, which offers a representative estimate for the spanwise scale of the streaks. This localisation indicates that only streaks sufficiently close to the observable point contribute meaningfully to the instantaneous skin friction, whereas the majority of remote structures produce a negligible contribution. Note that although the decomposition is performed using an observable at a single wall location, this does not reduce generality because the underlying flow is statistically homogeneous in both x and z .

To better show the structures of the resulting CCD modes, three-dimensional isosurface visualisations are shown in figure 4. These renderings reinforce the picture obtained from the planar views: the dominant CCD structures manifest as localised, streamwise-elongated streaks anchored to the vicinity of the observable point on the wall. In addition, for streaks aligned with the channel centreline, a symmetric pair of structures is observed on either side, each with comparable scale but opposite phase. This pairing behaviour is consistent with the reflectional symmetry of the channel geometry and with the tendency of near-wall streaks to form in counter-rotating or phase-opposed arrangements as part of the self-sustaining cycle. Such paired streaks have been associated with the flanking motions induced by quasi-streamwise vortices, which naturally generate alternating high- and low-speed regions.

In contrast, the first POD mode shown in figure 5 also appears as a streamwise-elongated streak, but it is neither centred around the observer location nor localised in the spanwise direction. This behaviour is expected because POD prioritises structures that maximise kinetic-energy, rather than those most strongly associated with c_f variations. The 2nd- to the 4th-order POD modes are similar to the first modes hence omitted.

As mentioned in section 1, the skin-friction-producing structures are also known to vary with Reynolds number. To assess these changes, CCD is applied to a turbulent channel flow at a higher friction Reynolds number, $Re_\tau \approx 550$. The resulting first four leading-order CCD modes are shown in figure 6. Compared with $Re_\tau \approx 180$ case, the mode shapes retain a broadly similar organization and spatial distribution, suggesting that the underlying mechanism of skin-friction production remains qualitatively unchanged. Nevertheless, notable differences also exist. In particular, the streamwise extent of the structures becomes significantly shorter, consistent with the well-established trend of decreasing characteristic length scales as Re_τ increases.

The 3D visualisations in figure 7 further demonstrate that the CCD structures decrease in size both in x and z directions. A key difference, evident in figure 7(a), is that the pair of opposite-phase streaks flanking the primary streak becomes much weaker compared with figure 4(a), suggesting that at higher Reynolds numbers, the streaks are spanwisely less uncorrelated. To evaluate whether low-rank behaviour persists at higher Reynolds numbers, the skin friction is reconstructed using the leading CCD modes. The CCD spectra and reconstruction results are shown in figure 8. Although the decay of σ_j^2 is somewhat slower than in the $Re_\tau \approx 180$ case, the first few singular values still decrease rapidly, indicating

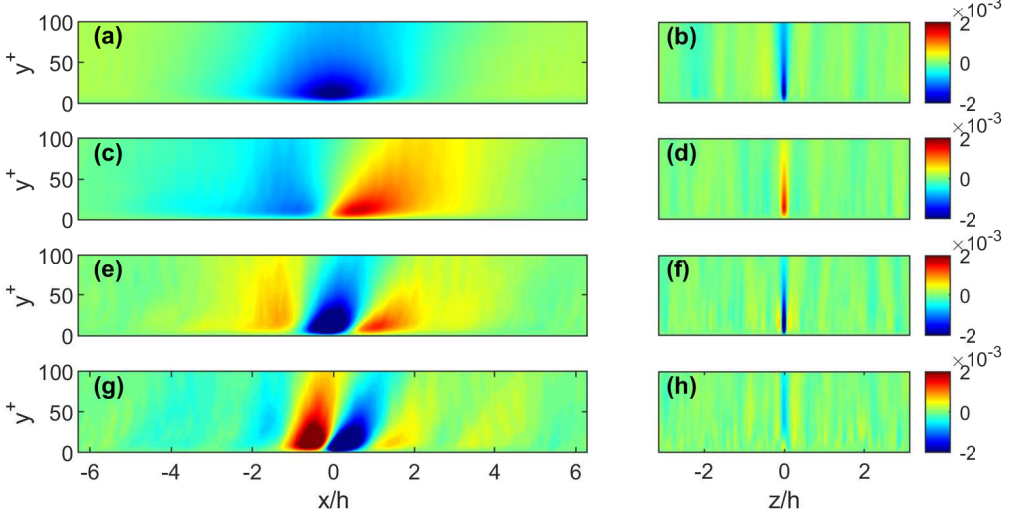


Figure 6: Front (a, c, e, g) and left (b, d, f, h) views of the first four CCD modes when $Re_\tau \approx 550$. $z = 0$ for (a, c, e, g) while $x = 0$ for (b, f) and $x = 1/3\pi$ for (c, h).

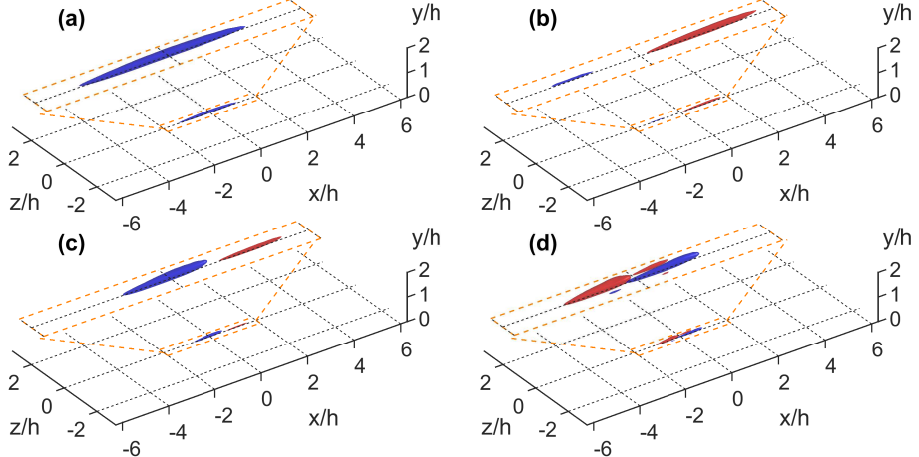


Figure 7: Isosurface of the 1st- to 4th-order (a to d) CCD modes when $Re_\tau \approx 550$. The red and blue isosurfaces represent 50% and -50% of the fluctuation amplitude, respectively. Structures are zoomed-in in orange boxes ($-2 < x < 2$, $-0.25 < z < 0.25$).

a possibility of low-rank behaviour. Consequently, reconstruction of the instantaneous skin friction using only the first four CCD modes remains effective, as demonstrated in figure 8(b). These results confirm that the leading CCD modes at $Re_\tau \approx 550$ continue to represent the dominant flow features responsible for skin-friction production.

To measure the contribution of each CCD mode in the skin friction reconstruction when Re_τ varies, we define the contribution ratio of the k -th order mode as $a_k^2(t)/\sum_{n=1}^4 a_n^2(t)$, and the results are shown in figure 9. For both $Re_\tau \approx 180$ and 550, the first-order mode accounts for more than 40% of the reconstructed skin friction, indicating its leading role. As Re_τ increases, the second-order mode appears to exhibit a more pronounced effect. It is worth noting that the sampling frequency of the observable should be increased for a better mode convergence and hence a more conclusive demonstration of this trend at $Re_\tau \approx 550$.

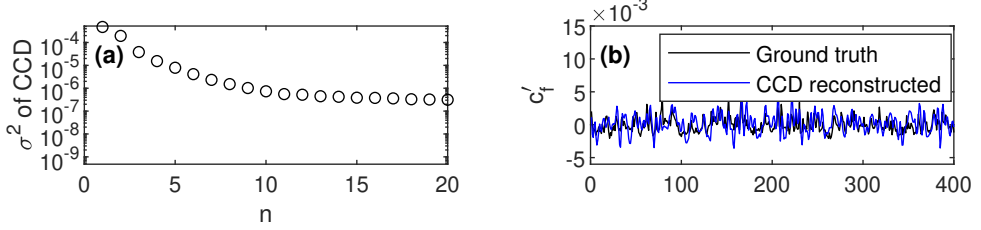


Figure 8: (a) The CCD spectra and (b) reconstruction of c_f for the $Re_\tau \approx 550$ case.

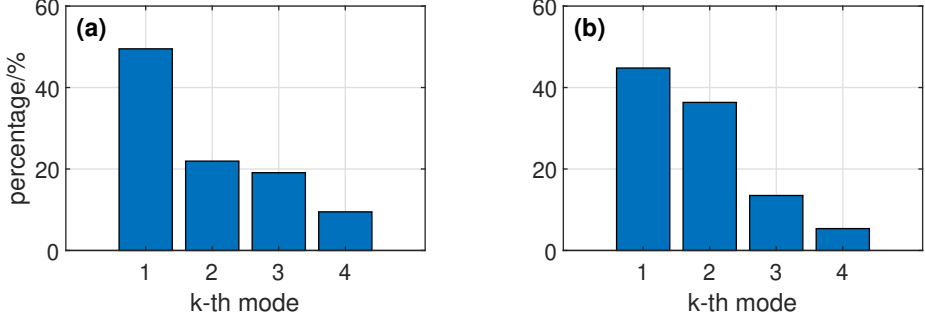


Figure 9: Modal contribution in flow reconstruction, when (a) $Re_\tau \approx 180$ and (b) 550.

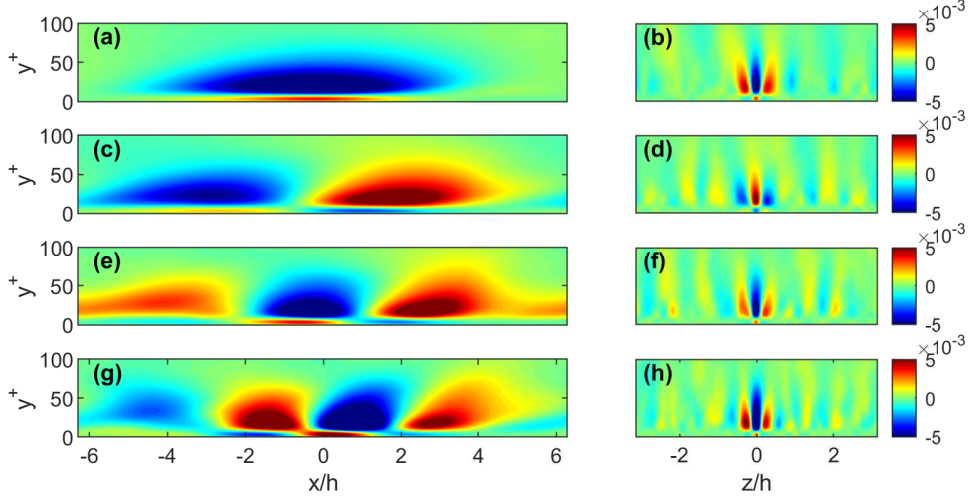


Figure 10: Front (a, c, e, g) and left (b, d, f, h) views of the first four CCD modes for the controlled channel flow. $z = 0$ for (a, c, e, g), while $x = 0$ for (b, f) and $x = 1/3\pi$ for (c, h).

3.2. Case of $Re_\tau \approx 180$ with opposition controls

To examine the mechanism of opposition control, we apply the CCD to the controlled database at $Re_\tau \approx 180$. An examination of the mean skin friction shows that a total reduction of 22% is achieved. The first four CCD modes for this case are shown in figures 10–11. Similar to the uncontrolled cases, the dominant structures retain a streaky characteristics; however, their spatial organisation undergoes substantial modification. Most notably, the streaks are lifted farther away from the wall and show a pronounced reduction in streamwise extent. For the

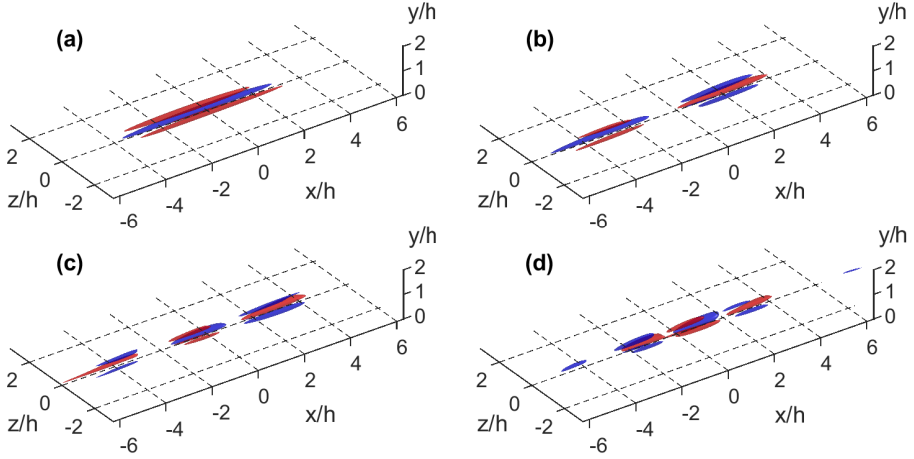


Figure 11: Isosurface of the 1st- to 4th-order (a-d) CCD modes for controlled flow. The red and blue isosurfaces represent 50% and -50% of the fluctuation amplitude, respectively.

leading-order mode, the streamwise length of the primary streak reduces from approximately $12h$ in the uncontrolled case (figure 3(a)) to about $8h$ under control (figure 10(a)). A more significant structural change is the emergence of a secondary streak immediately beneath the primary streak, as seen in figure 10. This secondary structure is thinner, shorter, and more compact—approximately half the streamwise length and one-third the spanwise width of the primary streak—and exhibits an opposite phase.

The 3D visualisations in figure 11 further highlight the reorganisation of flow structures induced by opposition control. The streak system appears more interwoven and segmented than in the uncontrolled case. In particular, the two lateral streaks flanking the primary streak become substantially more prominent—comparable in amplitude and spanwise width to the primary structure—whereas in the uncontrolled flow, they are noticeably weaker. This enhanced presence of side streaks, together with the lifted and shortened primary structure, indicates a redistribution of near-wall coherence that is consistent with the observed reduction in wall friction.

4. Conclusion

The new flow field decomposition method, Canonical Correlation Decomposition (CCD), is applied to turbulent channel flows to identify coherent structures most strongly associated with skin friction (c_f) generation. At $Re_\tau \approx 180$, c_f is found to correlate primarily with a set of streamwise-elongated streaks localised in the immediate spanwise vicinity of the observable point. The CCD spectrum exhibits a pronounced low-rank character: the first four modes capture more than 80% of the c_f variation, in stark contrast to the slow reconstruction using the POD modes.

When Re_τ increases to 550, the CCD modes retain the same qualitative streaky structures but contract in both streamwise and spanwise directions, consistent with the decrease of characteristic near-wall length scales at higher Reynolds numbers. Despite these quantitative differences, the underlying mechanism associated with streak-driven wall-shear production appears largely unchanged. The opposition-controlled case reveals a markedly different structural organisation. The primary streaks are lifted up from the wall and become shorter in the streamwise direction. More importantly, a secondary, thinner, and more compact streak of opposite phase emerges beneath each lifted streak. The three-dimensional visualisations further show a greater interweaving of streaks and enhanced prominence of flanking streaks, indicating a substantial reorganisation of near-wall coherent structures under control.

In summary, these results demonstrate that CCD provides a compact and physically interpretable framework for systematically isolating the flow structures responsible for the skin-friction generation and for quantifying how these structures change under various control techniques. The structural insights obtained here offer a promising route toward an improved understanding of drag-producing mechanisms and may inform the development of more effective drag-reduction techniques in wall-bounded turbulence in future works.

Funding. The authors wish to gratefully acknowledge the National Natural Science Foundation of China (NSFC) under grant numbers 12472263, U25700222.

Declaration of interests. The authors report no conflict of interest.

REFERENCES

CHEN, XI, YAO, JIE & HUSSAIN, FAZLE 2021 Theoretical framework for energy flux analysis of channels under drag control. *Physical Review Fluids* **6** (1), 013902.

ELNAHHAS, AHMED & JOHNSON, PERRY L 2022 On the enhancement of boundary layer skin friction by turbulence: an angular momentum approach. *Journal of Fluid Mechanics* **940**, A36.

FLORYAN, DANIEL 2023 A fundamental limit on energy savings in controlled channel flow, and how to beat it. *Journal of Fluid Mechanics* **954**, R3.

FUKAGATA, KOJI, IWAMOTO, KAORU & KASAGI, NOBUHIDE 2002 Contribution of reynolds stress distribution to the skin friction in wall-bounded flows. *Physics of Fluids* **14** (11), 73–76.

GATTI, DAVIDE & QUADRI, MAURIZIO 2016 Reynolds-number dependence of turbulent skin-friction drag reduction induced by spanwise forcing. *Journal of Fluid Mechanics* **802**, 553–582.

DE GIOVANETTI, MATTEO, HWANG, YONGYUN & CHOI, HAECHON 2016 Skin-friction generation by attached eddies in turbulent channel flow. *Journal of Fluid Mechanics* **808**, 511–538.

GAD-EL HAK, MOHAMED 2007 *Flow control: passive, active, and reactive flow management*. Cambridge University Press.

HWANG, YONGYUN 2015 Statistical structure of self-sustaining attached eddies in turbulent channel flow. *Journal of Fluid Mechanics* **767**, 254–289.

JEONG, JINHEE, HUSSAIN, FAZLE, SCHOPPA, WADE & KIM, JOHN 1997 Coherent structures near the wall in a turbulent channel flow. *Journal of Fluid Mechanics* **332**, 185–214.

KIM, JOHN 2011 Physics and control of wall turbulence for drag reduction. *Philosophical Transactions of the Royal Society of London A: Mathematical, Physical and Engineering Sciences* **369** (1940), 1396–1411.

LEE, MYOUNGKYU & MOSER, ROBERT D 2015 Direct numerical simulation of turbulent channel flow up to Re 5200. *Journal of Fluid Mechanics* **774**, 395–415.

LYU, B. 2024a Canonical correlation decomposition of numerical and experimental data for observable diagnosis. *ArXiv Preprint* p. arXiv:2312.14858.

LYU, B. 2024b Canonical correlation decomposition of numerical and experimental data for observable diagnosis. In *Proceedings of 30th AIAA/CEAs Aeroacoustics Conference*. AIAA 2024-3206.

MARUSIC, IVAN, CHANDRAN, DILEEP, ROUHI, AMIRREZA, FU, MATT K, WINE, DAVID, HOLLOWAY, BRIAN, CHUNG, DANIEL & SMITS, ALEXANDER J 2021 An energy-efficient pathway to turbulent drag reduction. *Nature communications* **12** (1), 5805.

RASTEGARI, AMIRREZA & AKHAVAN, RAYHANEH 2018 The common mechanism of turbulent skin-friction drag reduction with superhydrophobic longitudinal microgrooves and riblets. *Journal of Fluid Mechanics* **838**, 68–104.

RENARD, NICOLAS & DECK, SÉBASTIEN 2016 A theoretical decomposition of mean skin friction generation into physical phenomena across the boundary layer. *Journal of Fluid Mechanics* **790**, 339–367.

RICCO, PIERRE & SKOTE, MARTIN 2022 Integral relations for the skin-friction coefficient of canonical flows. *Journal of Fluid Mechanics* **943**, A50.

YAO, JIE, CHEN, XI & HUSSAIN, FAZLE 2018 Drag control in wall-bounded turbulent flows via spanwise opposed wall-jet forcing. *Journal of Fluid Mechanics* **852**, 678–709.

YAO, JIE, GARCÍA, EDGARDO & HUSSAIN, FAZLE 2025 Drag reduction via opposition control in turbulent channel flows at high reynolds numbers. *Physical Review Fluids* **10** (9), 094604.

YOON, MIN, AHN, JUNSUN, HWANG, JINYUL & SUNG, HYUNG JIN 2016 Contribution of velocity-vorticity correlations to the frictional drag in wall-bounded turbulent flows. *Physics of Fluids* **28** (8), 081702.

ZHAO, YUNCHAO, FAN, YITONG & LI, WEIPENG 2024 Reynolds number effects on a velocity–vorticity correlation-based skin-friction drag decomposition in incompressible turbulent channel flows. *Journal of Fluid Mechanics* **979**, A20.